AGU PUBLICATIONS

JGR

Journal of Geophysical Research: Space Physics

RESEARCH ARTICLE

10.1002/2013JA019301

Key Points:
- Terrestrial gamma ray flashes detected by the AGILE satellite are described
- The data set properties provide independent confirmation for key TGF properties
- A new technique for comparing different TGF data sets is presented and discussed

Correspondence to:
M. Marisaldi,
marisaldi@iasfbo.inaf.it

Citation:
Marisaldi, M., et al. (2014), Properties of terrestrial gamma ray flashes detected by AGILE MCAL below 30 MeV *J. Geophys. Res. Space Physics*, *119*, 1337–1355, doi:10.1002/2013JA019301.

Received 23 AUG 2013
Accepted 20 DEC 2013
Accepted article online 27 DEC 2013
Published online 20 FEB 2014

Properties of terrestrial gamma ray flashes detected by AGILE MCAL below 30 MeV

M. Marisaldi[1,2], F. Fuschino[1], M. Tavani[3,4], S. Dietrich[5], C. Price[6], M. Galli[7], C. Pittori[8,9], F. Verrecchia[8,9], S. Mereghetti[10], P. W. Cattaneo[11], S. Colafrancesco[9,12], A. Argan[13], C. Labanti[1], F. Longo[14,15], E. Del Monte[3], G. Barbiellini[14,15], A. Giuliani[10], A. Bulgarelli[1], R. Campana[1], A. Chen[10,12], F. Gianotti[1], P. Giommi[8], F. Lazzarotto[3], A. Morselli[16], M. Rapisarda[17], A. Rappoldi[11], M. Trifoglio[1], A. Trois[18], and S. Vercellone[19]

[1]INAF-IASF, National Institute for Astrophysics, Bologna, Italy, [2]Birkeland Centre for Space Science, University of Bergen, Bergen, Norway, [3]INAF-IAPS Roma, Rome, Italy, [4]Dipartimento di Fisica, Università Tor Vergata, Rome, Italy, [5]CNR-ISAC Roma, Rome, Italy, [6]Department of Geophysics and Planetary Sciences, Tel Aviv University, Tel Aviv, Israel, [7]ENEA, Bologna, Italy, [8]ASI Science Data Center, Rome, Italy, [9]INAF-OAR, Rome, Italy, [10]INAF-IASF Milano, Milano, Italy, [11]INFN Pavia, Pavia, Italy, [12]School of Physics, University of the Witwatersrand, Johannesburg, South Africa, [13]INAF, Rome, Italy, [14]Dipartimento di Fisica, Università di Trieste, Trieste, Italy, [15]INFN Trieste, Trieste, Italy, [16]INFN Roma "Tor Vergata", Rome, Italy, [17]ENEA Frascati, Rome, Italy, [18]INAF-Osservatorio Astronomico di Cagliari, Capoterra, Italy, [19]INAF-IASF Palermo, Palermo, Italy

Abstract We present the characteristics of 308 terrestrial gamma ray flashes (TGFs) detected by the Minicalorimeter (MCAL) instrument on board the AGILE satellite during the period March 2009–July 2012 in the $\pm 2.5^{\circ}$ latitude band and selected to have the maximum photon energy up to 30 MeV. The characteristics of the AGILE events are analyzed and compared to the observational framework established by the two other currently active missions capable of detecting TGFs from space, RHESSI and Fermi. A detailed model of the MCAL dead time is presented, which is fundamental to properly interpret our observations. The most significant contribution to dead time is due to the anticoincidence shield in its current configuration and not to the MCAL detector itself. Longitude and local time distributions are compatible with previous observations, while the duration distribution is biased toward longer values because of dead time. The intensity distribution is compatible with previous observations, when dead time is taken into account. The TGFs cumulative spectrum supports a low production altitude, in agreement with previous measurements. We also compare our sample to lightning sferics detected by the World Wide Lightning Location Network and suggest a new method to assess quantitatively the consistency of two TGF populations based on the comparison of the associated lightning activity. According to this method, AGILE and RHESSI samples are compatible with the same parent population. The AGILE TGF catalog below 30 MeV is accessible online at the website of the ASI Science Data Center http://www.asdc.asi.it/mcaltgfcat/.

1. Introduction

Terrestrial gamma ray flashes (TGFs) are intense and brief pulses of gamma rays associated with thunderstorm activity, currently detected mostly from space by detectors designed for astrophysical purposes. A detailed review of TGFs and associated phenomena is reported in *Dwyer et al.* [2012]. Since their discovery in the early 1990s by the Burst and Transient Source Experiment (BATSE) detector on board the NASA Compton Gamma Ray Observatory [*Fishman et al.*, 1994], a wealth of observations have been provided by the three currently operative space instruments capable of TGF detection: the Reuven Ramaty High Energy Solar Spectroscopic Imager (RHESSI) [*Smith et al.*, 2005], the Gamma Ray Burst Monitor (GBM) on board the Fermi satellite [*Briggs et al.*, 2010], and Astrorivelatore Gamma ad Immagini Leggero (AGILE) [*Marisaldi et al.*, 2010a]. RHESSI has provided the largest TGF data set available up to now. The first RHESSI TGF catalog includes 820 TGFs detected between March 2002 and February 2008 [*Grefenstette et al.*, 2009], with an average detection rate of $\approx$ 11 TGFs/month. *Gjesteland et al.* [2012] introduced an improved data selection algorithm which increased by a factor of 2 the RHESSI TGF sample, unveiling faint events unrecognized by the previous selection. Preliminary TGF detections by Fermi GBM were limited to a rate of $\approx$ 1 TGFs/month by the on-board trigger logic active on a minimum time scale of 16 ms [*Briggs et al.*, 2010]. Since November 2009, a change in the trigger algorithm resulted in an increase in the detection rate up to 8 TGFs/month [*Fishman et al.*, 2011], but the breakthrough came recently with the introduction of an untriggered data

collection mode active on specific geographic regions that allowed the detection of 384 TGFs during 1037 h of observation [*Briggs et al.*, 2013]. Since November 2012 this operative mode is enabled for the entire Fermi orbit and should result in the detection of about 850 TGFs/yr [*Briggs et al.*, 2013]. In this paper we present the characteristics of 308 TGFs detected by AGILE in the period March 2009–July 2012, with an average detection rate of $\approx$ 10 TGFs/month.

The availability of large TGF data sets spanning several years and geographical regions is crucial for correlation with other satellite and ground-based observations and sets the basis for the first TGF climatology studies. The comparison between TGFs and lightning flash density derived by the observations of the Lightning Imaging Sensor instrument on board the Tropical Rainfall Measuring Mission (TRMM) satellite evidenced a geographical dependence of the TGF/lightning flash ratio. This result has been confirmed independently using TGF samples from RHESSI [*Smith et al.*, 2010], AGILE [*Fuschino et al.*, 2011] and Fermi GBM [*Briggs et al.*, 2013]. The correlation between TGFs and radio atmospheric signals (sferics) detected by the World Wide Lightning Location Network (WWLLN) is a common practice to provide evidence of the lightning activity characteristics of the thundercloud where the TGF is produced and for one-to-one correlations capable to unveil the relation between TGF and the lightning process [*Connaughton et al.*, 2013]. *Østgaard et al.* [2013] report a TGF and the optical emission by the associated lightning discharge observed by two different spacecrafts (RHESSI and TRMM) crossing the same region at the same time. This work, and the reconstruction of the full sequence of events from leader initiation, TGF production, lightning stroke, and optical flash, would not have been possible without the availability of the improved RHESSI TGF catalog presented in *Gjesteland et al.* [2012].

All these advancements have been boosted by the availability of large high-confidence TGF data sets. However, a good understanding of the similarities and differences between TGF samples observed by different satellites is crucial to understand the possible biases involved in the use of one particular sample. These differences can in turn be ascribed to the differences in the detectors and observation conditions, such as the covered geographical region.

Although the presence of TGF photons with energies up to several tens of MeV had already been established [*Smith et al.*, 2005; *Marisaldi et al.*, 2010a; *Briggs et al.*, 2011], in *Tavani et al.* [2011a] our team has shown that the AGILE TGF cumulative spectrum at high energy deviates from a power law with exponential cutoff model and can be better fit with a broken power law with significant counts above background up to ~100 MeV. The AGILE silicon tracker detected TGF high-energy photons above 20 MeV (average energy 60 MeV) and localized them within a region clustered around the subsatellite point (i.e., the point on the Earth surface corresponding to the nadir of the spacecraft), as reported in *Marisaldi et al.* [2010b]. Moreover, as statistics grew up, we realized that our TGF sample is possibly composed by two distinct populations: a low-energy population, consistent with typical TGF characteristics, and a high-energy population, with quite distinct features [*Tavani et al.*, 2011b; *Marisaldi et al.*, 2012]. The fraction of the high-energy TGFs amount to $\approx$ 15% of the total number of transients satisfying the selection criteria for TGF defined in *Marisaldi et al.* [2010a]. This population becomes dominant for energies above ~30 MeV, where a break in the cumulative spectrum is observed. *Celestin et al.* [2012] shows that this high-energy component is compatible with electron acceleration in non-homogeneous electric fields at lightning leader tips; however, *Briggs et al.* [2013] suggests that it could also be explained by cosmic ray contamination of the TGF sample. Given the current status of the analysis, we can exclude this latter possibility for most of the high-energy events. The existence of TGFs with photon energy up to 100 MeV poses severe constrains to TGF production models and deserves a dedicated discussion that will be reported in a forthcoming paper. In this paper we consider only TGFs with photon maximum energy $\leq$ 30 MeV.

2. Instrument and Data Description

AGILE [*Tavani et al.*, 2009] is a space mission of the Italian Space Agency (ASI) devoted to astrophysics in the gamma ray energy range 30 MeV–30 GeV and in the X-ray band 18 keV–60 keV. AGILE was launched on 23 April 2007 in a low-Earth orbit at 550 km altitude with 2.5° inclination, and at the time of writing it has completed its sixth successful year of operations in orbit. The AGILE payload is composed of a tungsten-silicon tracker (ST) [*Prest et al.*, 2003], for gamma-ray imaging in the energy range 30 MeV – 30 GeV; a silicon based X-ray detector, SuperAGILE (SA) [*Feroci et al.*, 2007], for imaging in the range 18 keV – 60 keV; a CsI(Tl) mini-calorimeter (MCAL) [*Labanti et al.*, 2009] for the detection of gamma-rays in the range

300 keV – 100 MeV; and an anticoincidence (AC) system [*Perotti et al.*, 2006] made with plastic scintillator layers for the rejection of charged particles. The scientific payload is completed by the Payload Data Handling Unit (PDHU) [*Argan et al.*, 2004] that takes care of data acquisition of the various detectors. ST and MCAL form the Gamma-Ray Imaging Detector (GRID) for observations in the energy range 30 MeV–30 GeV.

We have already demonstrated the capability to detect TGFs with the GRID, providing the first direct localization of TGFs in gamma rays [*Marisaldi et al.*, 2010b]. However, due to the instrument setup and observation strategies, GRID detections are quite rare, and most of the TGFs are detected by MCAL alone. In the following we will refer only to TGFs detected by MCAL.

MCAL is composed of 30 CsI(Tl) scintillator bars ($15 \times 23 \times 375$ mm^3) each read out by two custom PIN Photodiodes (PD) coupled at the two small sides. The bars are arranged in two orthogonal layers, for a total thickness of 1.5 radiation lengths. MCAL can work both in conjunction with the ST (GRID operative mode), helping for event selection and energy reconstruction, and as a stand-alone all-sky transient monitor in the 350 keV–100 MeV energy range (burst operative mode). Both operative modes are active at the same time. In the BURST operative mode an onboard trigger logic is active on several time scales spanning 4 orders of magnitude from 8 s down to 293 μs, allowing the detection of a wide variety of transient phenomena from long cosmic Gamma Ray Bursts (GRBs) to TGFs at submillisecond time scale. When a trigger is issued, MCAL data are sent to telemetry on a photon-by-photon basis for a several seconds long time window centered at the trigger time, including, for each photon, energy information and a time tag with 2 μs accuracy. The BURST operative mode is the one relevant for TGF detection. The trigger logic parameters for every time window, including threshold level, background integration time, data time interval to be sent to telemetry, are fully configurable via onboard software. *Labanti et al.* [2009] reports the full description of the instrument; *Fuschino et al.* [2008] describes the details of the onboard trigger logic; *Marisaldi et al.* [2008] and *Galli et al.* [2013] report the GRB detection capabilities and results.

Timing accuracy at the microsecond level is a crucial characteristic of a TGF detector, given the very short duration of TGFs and the importance of cross-correlation with other satellite or on-ground lightning measurements. In fact, cross correlation of gamma ray light curves with extremely low frequency and very low frequency (VLF) signals associated to lightning provides insight in the sequence of events linking TGF production and lightning activity. RHESSI has a timing uncertainty of $\approx$ 1.8 ms, which can be further reduced to ~400 μs using correlation with sferics detected by WWLLN [*Østgaard et al.*, 2013]. Both Fermi and AGILE onboard time is synchronized to UTC by the Global Positioning System (GPS) time sampled at a rate of 1 Hz. The AGILE onboard clock deviations from the GPS reference are of order of few μs per second and are corrected for by on-ground data preprocessing. MCAL data are also routinely used within the third Inter-Planetary Network (IPN, web page: http://www.ssl.berkeley.edu/ipn3/) for GRB localization by means of triangulation, see *Hurley et al.* [2013] and *Pal'shin et al.* [2013] for recent IPN results including MCAL data. *Pal'shin et al.* [2013] used timing data for 23 precisely localized GRBs to test the accuracy of the localization algorithm. In the case of the short bright GRB 090510 the difference between the observed and expected time delay between MCAL and the Konus-WIND spacecraft is $1.5^{+1.3}_{-3.3}$ ms (1σ error), as resulting from the cross correlation of the burst light curves (V. Pal'shin, personal communication, 2013). Although larger than the nominal timing accuracy, this measurement provides an independent upper limit to it and an end-to-end verification of the timing information and spacecraft ephemeris retrieval software.

3. Trigger Algorithm and Selection Criteria

The onboard trigger logic acts on several time windows spanning from 293 μs up to 8 s. The time windows relevant to TGF search are the 293 μs, 1 ms, and 16 ms windows, for which static (i.e., not related to background variation) threshold of 8, 10, and 22 counts were set, respectively. When a trigger is issued, all MCAL counts in a time interval centered at the trigger time are sent to telemetry on a photon-by-photon basis. The extension of this time interval was adjusted during the mission lifetime due to telemetry requirements but was never set shorter than 2 s for short time windows. The thresholds were kept as low as possible to maximize detection efficiency, but a large fraction of triggers can be ascribed to electronic noise contamination; therefore, a careful on-ground selection strategy was implemented. The trigger logic is active with this configuration since March 2009. All events reported in this paper were detected with such configuration. Previous detections already presented in *Marisaldi et al.* [2010a] (34 events) were based on a less sensitive configuration and are not included in the present work, in order to present a homogeneous sample.

The following selection algorithm was applied. All photon-by-photon data were scanned by means of a moving time window of 1 ms in duration. For every count a new time window is opened starting from the count time. If at least six counts are contained in the time window, the count group is defined as a *cluster*. A cluster is extended to include all counts whose time difference with respect to the previous count is less than or equal to 300 μs. This step is intended to include all photons belonging to a potential TGF and provide a preliminary estimate of the TGF duration. The 300 μs value is a compromise between the average time separation of ∼2.7 ms between background counts and the average TGF duration of a few hundreds of microseconds. When the end of a cluster is reached, its main parameters are stored to file for successive analysis. After this preliminary screening, we obtain more than 400,000 clusters in the period of interest.

We define the following criteria to associate a cluster to a regular TGF (with maximum photon energy $\leq$ 30 MeV):

1. Onboard trigger fired is within 20 ms from cluster start time;
2. Number of counts $\geq$ 10;
3. Hardness ratio HR $\geq$ 0.5, where HR is defined as follows:

$$\mathrm{HR} = \frac{\text{number of counts with } E \geq 1.4 \text{ MeV}}{\text{number of counts with } E < 1.4 \text{ MeV}}$$

4. At least one count in each of the four quadrants of MCAL, where a quadrant is defined as half a detection plane;
5. Maximum photon energy is $\leq$ 30 MeV;

This selection algorithm is an improved version of the one applied to the first AGILE TGF detections discussed in *Marisaldi et al.* [2010a]. Due to the small inclination orbit, the MCAL background count rate is stable within 20% along all the orbit except in the South Atlantic anomaly (SAA), where the background level increases rapidly. Although MCAL trigger logic is active also during the SAA passages, in order to obtain a homogeneous sample we excluded the events triggered in the SAA from our analysis. Conditions 1–3 are the same applied with the previous algorithm; in fact, condition 1 is substantially equivalent to requiring the event to be triggered by the onboard logic. Condition 4 is a simple topological rule that requires all parts of MCAL to be involved in a valid trigger. Conditions 3 and 4 guarantee rejection of spurious triggers due to electronic noise, which typically manifest as bursts of low-energy counts clustered on one side of the instrument only. Hardness ratio is a good proxy for the spectral shape of the events, when the limited number of counts prevents more refined spectral analysis, as in this case. However, given the intrinsic TGF spectral variability [*Østgaard et al.*, 2008; *Hazelton et al.*, 2009; *Grefenstette et al.*, 2009], condition 3 might introduce a bias toward faint hard events.

Condition 5 was applied to select the low-energy population of TGFs, as discussed in section 1. The 30 MeV energy threshold was chosen as the energy where the observed high-energy component becomes dominant. A simple energy threshold was chosen in order to keep the selection criteria as simple as possible and model independent. However, if the hypothesis of two populations with different spectral characteristics is correct, this choice may introduce contamination of the selected sample by events belonging to the high-energy population which do not have photons above the 30 MeV because of limited count statistics. To address this issue we performed a bootstrap analysis starting from a large sample of simulated TGFs. The TGF intensities were obtained by random extraction from the observed intensity distribution. For each simulated TGF, the photon's energy was then randomly extracted from the cumulative spectrum of the observed high-energy population. It was then counted how many simulated TGFs do not have any photon with energy above 30 MeV and therefore would be selected by the criteria reported above. The simulations show that $\approx$ 13% of the selected events can in fact belong to the high-energy population. Lowering the energy threshold for condition 5 reduces the contamination, but then a larger fraction of the low-energy population is lost. A 30 MeV threshold represents a good compromise with this regard. This contamination cannot be removed unless a careful study of the high-energy events is carried out, which will be the scope of a forthcoming work.

The selection algorithm is fully automatic and, with respect to the previous one, more reliable because no visual inspection is required. This algorithm selected 308 events in the period March 2009–July 2012. Several attempts were made to further relax the selection criteria for triggered events, specifically concerning the number of counts and the hardness ratio. However, the longitude and local time distributions demonstrated

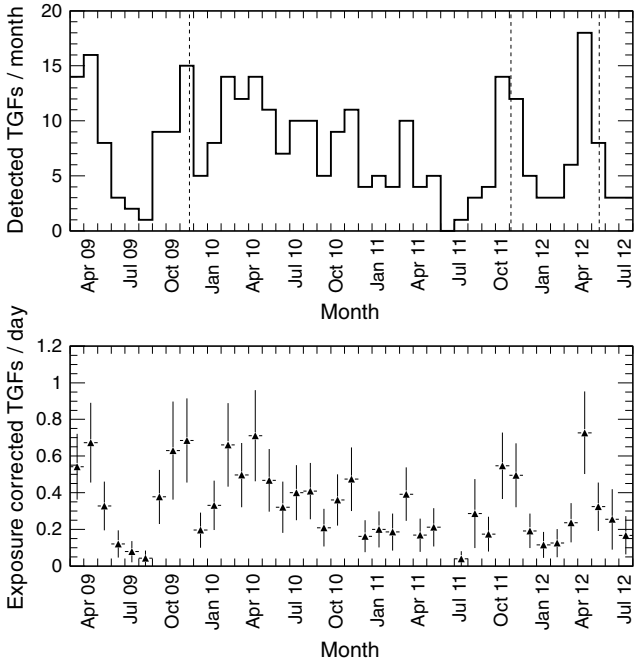

Figure 1. (top) AGILE TGF monthly detection rate. Dashed vertical lines, from left to right, mark AGILE entering spinning mode, and two successive MCAL energy threshold adjustments. (bottom) Daily TGF detection rate corrected for AGILE MCAL exposure.

that samples with relaxed conditions were contaminated by a large fraction of spurious triggers; therefore, this work focused on this high-confidence sample, although several low-fluence events were probably left undetected.

The data prescan in search of clusters was conceived with the basic idea to retrieve valid TGFs not detected by the trigger logic, possibly because they took place while another trigger had already been issued. This search is motivated by the fact that we have a large amount of photon-by-photon data available related to spurious triggers which may hide valid TGFs. This search yielded 49 additional events unrelated to an onboard trigger, i.e., satisfying all conditions reported above but 1. However, a careful analysis of the main distributions associated to this class of untriggered events suggests that the sample is highly contaminated by events due to electronic noise and it will not be further considered in this paper. The limited number of these untriggered events compared to the main sample makes us confident that, given the chosen set of criteria on the number of counts and hardness ratio, the selected sample of triggered events is rather reliable.

Figure 1 reports the monthly raw TGF detection rate (top) and the daily TGF detection rate (bottom) corrected for the monthly MCAL exposure, i.e., the effective time the detector and its trigger logic was active. In the considered period MCAL TGF detection rate is $\approx$ 10 TGFs/month, i.e., $\sim$0.3 TGFs/d, when exposure is accounted for. The variability in the monthly detection rate accounts for seasonal variability in thunderstorm activity across the equator. Dashed vertical lines in the top panel indicate three critical moments in MCAL activity and data acquisition. In October 2009, due to a failure of the reaction wheel, AGILE ended operations in pointing mode, i.e., observing the same sky region for observation blocks about 2 weeks long, and began working in spinning mode, i.e., spinning around the satellite-Sun vector with an average angular speed of $\approx$ 0.8°/s observing a large fraction of the sky every day. Given the TGF very short duration and hard spectrum, this change did not alter the detection efficiency. In October 2011 and April 2012 the energy threshold of MCAL was changed from about 350 keV to 450 and 500 keV, respectively. This action was necessary to cope with the increased electronic noise of MCAL and telemetry requirements.

TGFs triggered different combinations of the various time windows checked by the onboard trigger logic. The frequencies of the triggered time window configurations are reported in Table 1. About 92% of the events trigger on either the submillisecond (293 μs) or the 1 ms time window, or both of them.

Table 1. Hardware Trigger Configuration Fraction

16 ms	1 ms	293 μs	Fraction
		X	0.16
	X		0.23
	X	X	0.20
X			0.08
X		X	0.12
X	X		0.10
X	X	X	0.11

The submillisecond time window triggers about 60% of the events, while the 16 ms only configuration accounts for less than 8% of the events. Although being quite obvious, given the typical TGF time scale, these results can provide valuable input when designing a trigger logic tailored to TGF detection.

4. MCAL Dead Time Estimate

Instrumental dead time, i.e., the time during which a detector is not responsive to input pulses because busy in processing previous events, is a key characteristic of a radiation detector. The effect of dead time increases with the input event rate. This is particularly the case of TGFs, where a large fluence (≈ 0.1 cm^{-2}) is delivered in very short times (≈ 100 μs). All detectors that observed TGFs up to now are substantially affected by dead time [*Grefenstette et al.*, 2008, 2009; *Briggs et al.*, 2010; *Gjesteland et al.*, 2010], therefore a careful analysis of dead time effects in MCAL is mandatory.

The three main contributions to MCAL dead time are as follows: (i) the processing time of a single scintillation detector, (ii) the dead time induced by the anticoincidence (AC) shield, and (iii) the possible queuing of counts in the first-in first-out (FIFO) register that interfaces the instrument to the Payload Data-Handling Unit.

The interface FIFO register is a possible bottleneck because the maximum allowed count rate is limited by the throughput of the software task that handles data transmission between the instrument and the data-handling unit. If the FIFO is half full no more counts can be collected until the register has been emptied. However, the FIFO depth allows the storage of 500 events before issuing a FIFO half-full alert signal. We have never observed such a large number of counts followed by a gap in our data, so we can neglect this effect.

Each scintillating bar requires 20 μs for a photon acquisition, after the discriminator has fired. MCAL consists of 30 detectors each of them acting as an independent nonparalyzable detector. Due to this large degree of segmentation, detector's induced dead time would be significant for a number of counts much larger than what is commonly observed as, for example, ≈ 150 counts detected in ≈ 100 μs.

According to these considerations, the AC dead time should be the dominant contribution. Each AC pulse opens a 5.4 μs wide veto time window for MCAL, independent on the energy released in the detector, in order to properly reject the counts on all detectors which may exhibit small differences in time constants. In normal conditions, the AC rate is stable at a few kHz rate, leading to a dead time of a few percent. However, AC panels are sensitive in the hard X-ray range as is clearly evident looking at the AC rate during cosmic gamma ray bursts or solar flares. Moreover, high-energy photons interacting with either the detectors or the satellite structure may lead to the production of secondary charged particles that can interact in an AC panel leading to a veto signal. The AC is a paralyzable detector: every AC pulse opens a new veto window, regardless of its time distance from the previous pulse. This means that a sufficiently high flux may decrease the live time fraction to 0%. This is commonly observed when AGILE enters the SAA or during bright solar flares, when the MCAL ratemeters drop to zero due to dead time suppression. Unfortunately, the AC ratemeters are recorded on board with a 1 s time bin only, too coarse to measure this effect at the millisecond level.

We addressed the issue of AC-induced dead time by means of dedicated Monte Carlo simulations using the full AGILE mass model. The Monte Carlo code used is the full AGILE simulation code [*Longo et al.*, 2002; *Cocco et al.*, 2002] based on the simulation toolkit GEANT3 [*Brun and Carminati*, 1993], modified to include the specific MCAL detector parameters measured during calibration campaigns (scintillator detectors light yield and light attenuation coefficients [*Labanti et al.*, 2009]). All standard electromagnetic physics processes are included in the simulation. As TGF input spectrum we used the unfolded spectrum published in *Dwyer and Smith* [2005, Figure 1] (J. R. Dwyer and D. M. Smith, personal communication, 2013) for a source region placed at an atmospheric depth of 50 g/cm^2, corresponding to a production altitude of 21 km, which provides the best fit to the RHESSI TGF cumulative spectrum [*Dwyer and Smith*, 2005]. We simulated TGF spectra for different off-axis angles, and retrieved the number of counts detected in the AC above the energy threshold (100 keV) and the number of counts detected in MCAL above the energy threshold (350 keV). We then consider a TGF as parameterized by two main observables: its fluence at satellite altitude F and its duration

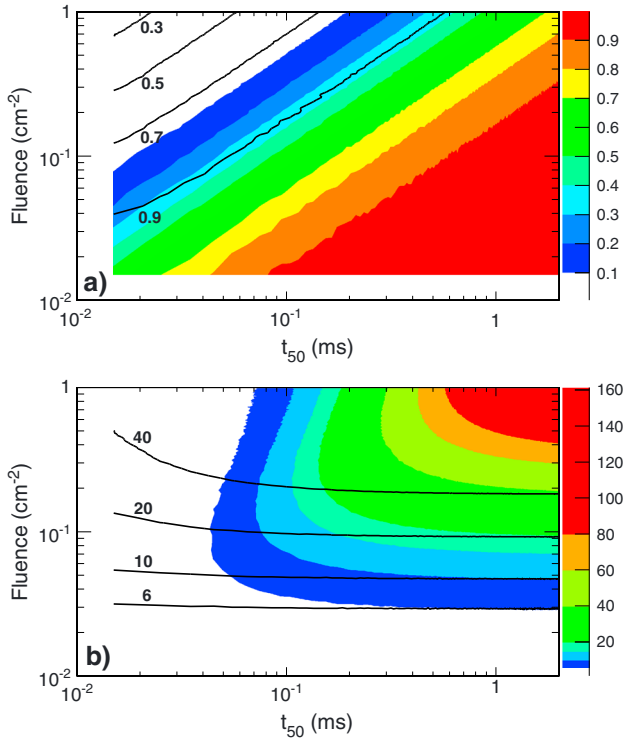

Figure 2. (a) Efficiency ε, i.e., the fraction of detected counts; (b) number of counts detected N^{obs} after dead time is taken into account, as a function of the true TGF duration and fluence, for TGFs detected 60° off-axis angle. Color scale: AC-induced dead time only. Black line contour: MCAL-induced dead time only.

expressed in terms of t_{50}, i.e., the time interval that includes the central 50% of the counts, described in details in section 5.2. We then generated 10^7 simulated TGFs in order to uniformly sample the parameter space given by (0.01 ms $< t_{50} <$ 2 ms) × (0.01 cm^{-2} $< F <$ 1 cm^{-2}). For each simulated TGF the expected number of counts in AC and in MCAL were defined according to F and the simulation results; the time series of the counts were randomly extracted according to a Gaussian time profile with $\sigma = 0.74\, t_{50}$. We then apply to the MCAL time series the effect of the dead time induced by the AC, rejecting all MCAL counts within the 5.4 μs time interval after an AC count. For each simulated TGF we then register the number of counts N^{obs} detected by MCAL after dead time was taken into account, and the efficiency ε, i.e., the fraction of detected counts with respect to the total number of counts, that is a good approximation of the live time fraction. The dead time fraction is then $(1 - \varepsilon)$. In order to check the hypothesis that the contribution to the dead time fraction induced by the MCAL detector processing time is negligible with respect to the AC contribution, we also simulated the MCAL contribution stand alone, i.e., assuming the AC is switched off, by rejecting all MCAL counts that take place within a 20 μs time interval following a count on the same scintillating bar.

Figure 2 shows $\varepsilon(t_{50}, F)$ and $N^{obs}(t_{50}, F)$ for an off-axis angle of 60°. The color scale refers to AC-induced dead time only, while black line contour refers to MCAL-induced dead time only. From Figure 2 (top) it is evident that the efficiency decreases; hence, the dead time fraction increases, as F increases and t_{50} decreases, as expected. TGFs with $t_{50} \sim 100$ μs have dead time fraction larger than 50% for fluences larger than 0.08 cm^{-2}. The dark blue contour band in Figure 2 (bottom) indicates the region where $6 \leq N^{obs}(t_{50}, F) < 10$, i.e., where a cluster should be recognized by the first step of the selection algorithm described in section 3 but not validated by the subsequent step. The white region indicates a region of the parameter space where a TGF can never be detected by MCAL because $N^{obs}(t_{50}, F) < 6$. It is evident that $F < 0.04$ cm^{-2} can never be detected, and for $t_{50} \sim 100$ μs the possibility of detection is marginal for any value of F. From Figure 2 it is also evident that the contribution to the dead time fraction due to the processing time of MCAL detectors is negligible with respect to the AC-induced contribution. Figure 2 (top) shows that the efficiency due to MCAL only is still 90% when it is already reduced to less than 30% by the AC contribution. Figure 2 (bottom) shows that, if only MCAL contribution to dead time were present, it would be possible to detect easily the TGFs with $t_{50} < 50$ μs, well within the region of the parameter space forbidden by the AC contribution. Owing to these results, in

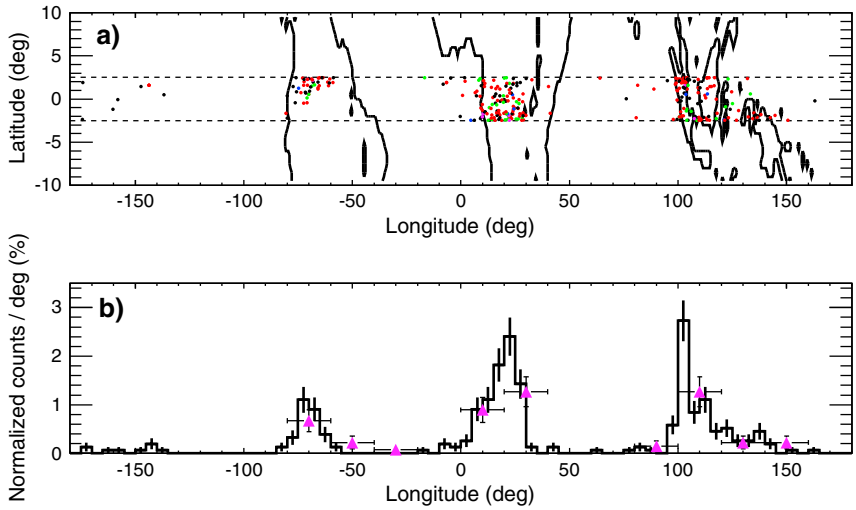

Figure 3. Geographical distribution of AGILE TGFs. (a) Scatterplot of the AGILE subsatellite points; the color indicates the hardness ratio of each event (black: HR < 1; red: 1 ≤ HR < 2; green: 2 ≤ HR < 3; blue: 3 ≤ HR < 4; magenta: HR ≥ 4). (b) Longitude distributions for 308 AGILE TGFs detected in 28 months (histogram) and 67 RHESSI TGFs (magenta filled triangles) detected in 46 months in the ±2.5° latitude band. The vertical axis error bars are 1 standard deviation assuming Poisson distribution.

the following discussion we will consider the contribution to dead time due to the AC only. For larger off-axis angles the dead time fraction becomes larger because it increases the ratio between events detected by the AC with respect to those detected by MCAL. In particular, backside illumination leads to high dead time fraction because of the Compton electrons and particles from pair production in the spacecraft, which may efficiently reach the AC panels. The dead time fraction has therefore important consequences on the detection of TGFs by MCAL, as discussed in details in the following section. In previous works we had already correctly identified the small contribution to the dead time fraction induced by the MCAL detectors. However, in this work we focus for the first time on the contribution of the AC, which turns out to be the major source of the dead time fraction of MCAL. Since the AC was specifically designed to reject charged particles, the AC-induced dead time also explains why no Terrestrial Electron Beam [*Dwyer et al.*, 2008; *Briggs et al.*, 2011] has been observed by AGILE.

5. Results and Discussion

5.1. Geographical and Local Time Distributions

Figures 3 and 4 show the geographical and local time distributions of the AGILE TGFs, respectively, compared to the equivalent distributions for 67 RHESSI events detected before 1 January 2006, in the ±2.5° latitude band, retrieved from the first RHESSI TGF catalog [*Grefenstette et al.*, 2009].

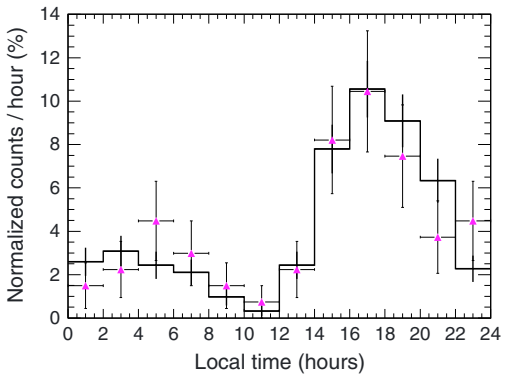

Figure 4. Local time distributions for AGILE (histogram) and 67 RHESSI (filled triangles) TGFs detected in the ±2.5° latitude band. The vertical axis error bars are 1 standard deviation assuming Poisson distribution.

TGF detection above Central America is clearly hampered by the SAA. The well-established clustering on continental masses and the occurrence peak in midafternoon are confirmed. The AGILE distributions are consistent with the RHESSI results, as previously pointed out [*Marisaldi et al.*, 2010a].

5.2. Duration Distribution

The limited number of counts per TGF makes it difficult to estimate the TGF duration by the t_{50} and t_{90} parameters, as done for the Fermi-GBM events in *Fishman et al.* [2011]. The t_{50} and t_{90} are defined as the time intervals including the central 50% and 90% of the counts in a transient events, respectively [*Koshut et al.*, 1996]. This is a reliable algorithm when the number of available counts is large, but fails when the statistics are limited, as in the case of AGILE TGFs. Therefore, we decided to estimate the duration of a

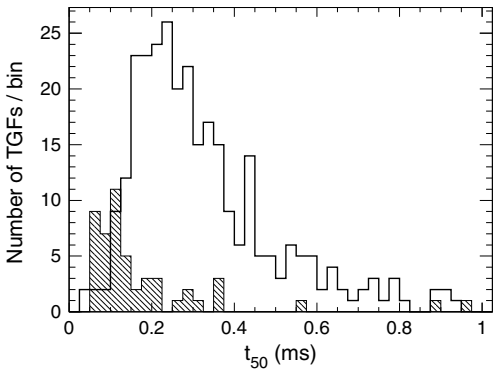

Figure 5. AGILE (continuous line) and Fermi-GBM (hatched histogram) TGF duration (t_{50}) distribution. Time bin is 25 μs.

TGF by fitting the event light curve with a Gaussian function and considering its standard deviation σ as a good estimator of the event duration. We applied a maximum likelihood algorithm to unbinned count time series, assuming a Gaussian function for the TGF signal and a constant background. The fit of the combined (signal and background) model was performed in a 20 ms time interval centered at the TGF trigger time. By the Gaussian function best fit parameters we can estimate both the duration and the intensity of the event.

For a Gaussian distribution, $t_{50} = 2\sqrt{2}\mathrm{Erf}^{-1}(0.5)\sigma \simeq 1.349\sigma$, where Erf($x$) is the error function. Similarly, $t_{90} \simeq 3.290\sigma$. Figure 5 shows the t_{50} distribution for AGILE events, together with that of Fermi-GBM reported in *Fishman et al.* [2011]. The median of the AGILE t_{50} distribution is 290 μs, and the average value is 370 μs. It must be noted that the typical duration is remarkably shorter than previously reported by this team concerning the first AGILE TGF detections [*Marisaldi et al.*, 2010a]. This is due both to the different method used to evaluate an event's duration and to the fact that most of our initial detections were biased toward long-duration events because of an issue on the trigger logic, fixed since March 2009. However, the new AGILE and Fermi-GBM t_{50} distributions remain remarkably different, the AGILE median being a factor of ~2.6 larger than that of Fermi-GBM [*Fishman et al.*, 2011; *Briggs et al.*, 2013]. This difference can be ascribed to the contribution of dead time, as discussed in section 4, that strongly inhibits the detection capability for short TGFs. This effect has also remarkable consequences concerning the search for sferics simultaneous to AGILE TGFs, as discussed in section 5.6.

5.3. Intensity Distribution

The true TGF fluence distribution is a key parameter to estimate the TGF to lightning flash ratio and therefore the overall global rate of TGFs. This in turn may have a significant impact on the overall amount of energy dissipated in the atmosphere by TGFs and finally on the TGF chemical impact. The true fluence distribution is obtained from the observed one with suitable assumptions on the source production altitude and instrument detection efficiency. Previous studies [*Collier et al.*, 2011; *Gjesteland et al.*, 2011; *Østgaard et al.*, 2012] have modeled the observed differential intensity distribution with a power law

$$\frac{dN}{dn} = A_0 n^{-\lambda} \tag{1}$$

where dN is the number of TGFs with observed number of counts in the interval dn and A_0 is a normalization factor. This is a reasonable assumption motivated by the good fit of RHESSI binned data obtained with such a model. Fitting AGILE binned intensity distribution between 10 and 40 counts yields an index $\lambda_{\mathrm{obs}} = 3.3 \pm 0.2$ and a reduced χ^2 of 1.05. However, according to *Crawford et al.* [1970] a power law fit to binned data is not the most accurate statistical method to estimate the model parameters and the consistency of experimental data with such a model. We therefore applied the maximum likelihood method to unbinned data, as described in *Crawford et al.* [1970], which makes full use of the data and provides an unbiased estimate of the exponent with the smallest error. We worked on the cumulative distribution $N(n)$, where $N(n)$ is the number of TGFs with $N^{\mathrm{obs}} \geq n$. If equation (1) holds, then $N(n)$ will be a power law with exponent $-\lambda + 1$. We tested different ranges of N^{obs}, and verified the goodness of fit by means of the one-sample Kolmogorov Smirnov (KS) test. We found that the full range $10 \leq N^{\mathrm{obs}} \leq 70$ cannot be described by a single power law (KS probability < 0.02). However for the range $18 \leq N^{\mathrm{obs}} \leq 70$ we obtain a good fit with $\lambda = 4.26 \pm 0.49$ and a KS probability of 0.98.

Østgaard et al. [2012] have shown that dead time significantly influences the observed counts distribution. Figure 6 shows the effects of dead time on the measured duration t_{50}^{obs} and N^{obs} of AGILE events, in the frame of the instrument dead time model described in section 4. Contour plots show the expected measured number of counts (equivalent to Figure 2, bottom) and the expected measured duration in the true (t_{50}, F) parameter space. Observed durations have been estimated calculating the standard deviation of the simulated photon time distribution after application of the dead time model. It is evident that for most observed durations (50% of the events have t_{50}^{obs} in the range 120–260 μs) there are two points in the (t_{50}, F)

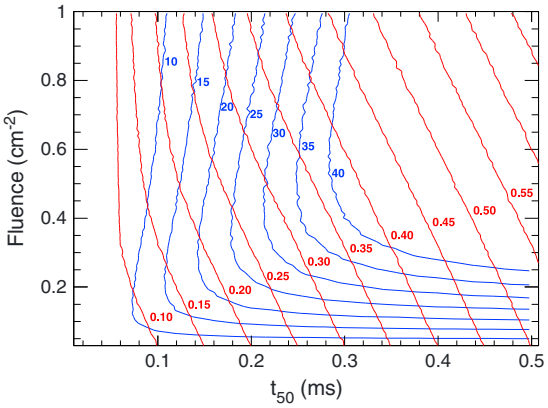

Figure 6. Contour plots of the number of detected counts N^{obs} (blue curves) and measured duration t_{50}^{obs} (red curves) in the true (duration, fluence) parameter space, assuming the dead time model discussed in the text.

space that lead to the same N^{obs}), i.e., the function that maps the (t_{50}, F) space into the (t_{50}^{obs}, N^{obs}) space is not injective and cannot be inverted. For example, a TGF with 20 observed counts and a measured duration of 200 μs could be either a TGF with fluence 0.15 cm^{-2} and true duration 180 μs or a brighter TGF with fluence 0.35 cm^{-2} and duration 150 μs. This is a direct consequence of the fact that the detector is paralyzable, i.e., for fluxes above a certain level, N^{obs} decreases. For this reason we cannot correct for dead time each observed TGF in order to retrieve F. We therefore applied a forward folding approach, starting from the expected true fluence distribution based on RHESSI and Fermi data [*Østgaard et al.*, 2012] and comparing the expected count distribution to the observed one after application of the dead time model.

To test the effects of dead time on the N^{obs} distribution, we built a population of simulated TGFs with fluences distributed according to equation (1) and duration distributed according to the Fermi TGF duration distribution reported in *Fishman et al.* [2011, Table 3]. For each generated TGF we then applied the following procedure:

1. Generate the count distribution for both MCAL and AC.
2. Add random uniformly distributed background counts to both MCAL (0.35 kHz) and AC (15 kHz).
3. Apply the dead time model, as described in section 4.
4. Fit the MCAL counts with the maximum likelihood technique as described in section 5.2 to estimate N^{obs}.

We then built the distribution of N^{obs} and compared it with the experimental one. The procedure is repeated for eight λ values in the range 1.9–2.6, spaced by 0.1. Two main assumptions are applied to these simulations. First, we consider the duration distribution reported in *Fishman et al.* [2011] as unbiased, therefore representing the true duration distribution for bright TGFs. This assumption is reasonable, considering the recent results by *Tierney et al.* [2013] indicating that TGF timing parameters are not significantly affected by dead time. However, it was decided not to use the duration distribution for untriggered TGFs reported in *Briggs et al.* [2013] because it corresponds to a population of faint, short-duration events, for which AGILE is less sensitive. *Briggs et al.* [2013] also show that the duration distribution of triggered and untriggered TGFs come from different distributions at the 99.8% confidence level. Moreover, we generated independently F and t_{50}, therefore assuming that these two parameters are uncorrelated. However, since also the dead time model is based on several assumptions, it is not worth to add further details to the simulation model at this stage.

Figure 7 shows the simulated N^{obs} cumulative distributions for $\lambda = 1.9$, 2.4, and 2.6, together with the experimental cumulative distribution. The bump features particularly evident for low values of N^{obs} are due to the discrete number of counts observed per TGFs and are remarkably well reproduced by simulations. We note that none of the simulated single power law distributions well matches the experimental data across the full counts range. This is due to the slope change evident in the experimental distribution for $\approx$ 18 counts, which is not reproduced by any single power law model. We assessed the consistency of experimental and simulated distributions by means of the two-sample KS test, as one of the most natural statistical tools to compare unbinned distributions. We applied the test to three counts intervals: 10–18, 18–70, and 10–70, including 221, 61, and 282 events, respectively. For each count interval and for each λ value we generated 1000 simulated data sets with the same number of events as the observed ones and computed the p value. We recall here that the p value indicates the probability of obtaining a maximum distance in the empirical cumulative distribution functions of the two samples larger than the observed one when the null hypothesis is verified, i.e., when the two samples are drawn from the same parent distribution. For the full (10–70) count intervals the p value for single power laws is typically lower than 0.05, and we can reject the null hypothesis at the 95% level. If we consider the 18–70 count interval the best match to experimental data is

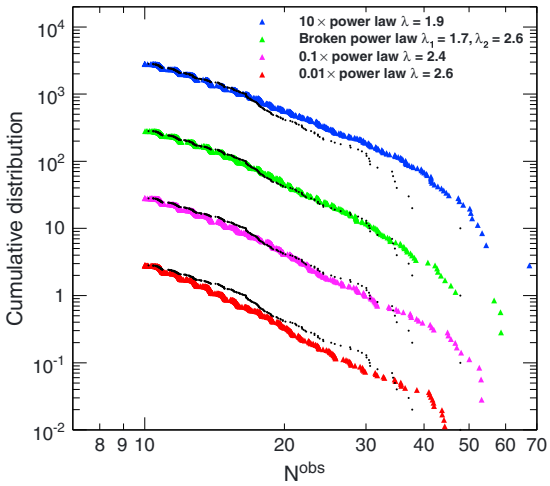

Figure 7. Black dots: experimental N^{obs} cumulative distribution. Filled triangles correspond to simulations of different initial intensity distributions, corrected for dead time and normalized to the observed number of counts. Plots are multiplied times scaling factors, for better clarity.

obtained for $\lambda = 2.4$, resulting in 88% of the trials with p value > 0.05. However, our method is not so sensitive, since λ values between 2.2 and 2.6 lead to similar results. *Tierney et al.* [2013] obtained a power law index $\lambda_F = 2.2 \pm 0.13$ for the intensity distribution of TGFs observed by Fermi-GBM, when dead time, pulse pileup, and detection efficiency are properly accounted for. It is remarkable that results from three different spacecrafts, with different characteristics and dead time models, point toward consistent results.

To account for the slope change at $\approx$ 18 counts, we also tested a true fluence distribution broken power law model with λ_1 and λ_2 power law indices for fluence lower and greater of a critical fluence F_c, respectively. Among several trials on the model parameters, the best results for the KS test in the three counts intervals described above is obtained for $\lambda_1 = 1.7$, $\lambda_2 = 2.6$, and $F_c = 0.15$ cm^{-2} (see also Figure 7). *Østgaard et al.* [2012] evidenced a possible roll-off for the lowest part of the RHESSI intensity distribution, which is best fit with a power law with $\lambda = 1.7$. Our observations apparently support this hypothesis. However, threshold effects related to the selection criteria, and not considered in these simulations, might affect the intensity distribution as well, resulting in the observed flattening for low N^{obs}. *Tierney et al.* [2013] do not find any evidence for a spectral flattening for low-intensity TGFs observed by Fermi-GBM. A large contribution to the corrected intensity distribution at low fluence values is given by detection efficiency. According to these results, we conclude that the slope change observed in AGILE TGFs can be due to the selection cut on hardness ratio, which was not modeled here because too many additional assumptions on TGF spectral shape and variability should have been made.

We also note that simulations described above produce a t_{50} distribution with a median (average) value of 180 (210) μs. This distribution is shifted toward larger t_{50} values than the parent distribution, as expected, but it is still different from the observed one. To obtain a distribution consistent with observations, it is necessary to assume a ratio between counts in the AC and in MCAL a factor $\approx$ 1.8 larger than that used here and based on Monte Carlo simulations of a typical TGF spectrum. This possibly means that we are underestimating the AC contribution to the dead time fraction, either because of a lower AC energy threshold or a larger contribution by scattering in the satellite bus.

5.4. Multiple Peaks

We observe seven groups of multiple peaks which are recognized as different TGFs by the selection algorithm. All groups include two peaks except the group on 22 November 2011, which includes three consecutive peaks. Table 2 reports the reference data for these events and the time separations between the consecutive peaks; Figure 8 shows the light curves for these events. The TGF identification number is in the form YYMMDD.DDDDD. If we fit the data using the unbinned maximum likelihood technique assuming a number of Gaussian peaks larger than two, we obtain a better likelihood for TGFs 090309.37239 and 111024.60597 when fit with four and three peaks, respectively, indicating that the selection algorithm may fail to identify dim closely spaced multiple peaks. By visual inspection of the light curves we identified several other potentially multipeaked events, with peaks separated by less than 300 μs, but in such cases we cannot exclude the effect to be an artifact due to dead time suppression of the central, high-flux part of the TGF, as described in *Gjesteland et al.* [2010].

If we assume the seven groups of events reported above consist of multiple bursts produced by a single TGF source, this kind of events accounts for about 2% of the AGILE sample. *Grefenstette et al.* [2009], in the analysis of 820 TGFs belonging to the first RHESSI TGF catalog, do not report any case of multiple peaks and explicitly state that TGFs are mostly isolated events. In the new RHESSI TGF sample, including a sample almost 3 times larger [*Gjesteland et al.*, 2012] few examples of double-peaked TGFs have been found

Table 2. TGFs With Multiple Peaks Within 10 ms

TGF ID	Date	Time (UT)	Lon. (deg)	Lat. (deg)	Δt (ms)
090309.37239	9 Mar 2009	08:56:15.207	−6.65	1.89	1.46
091011.64173	11 Oct 2009	15:24:06.362	29.80	−1.90	0.91
091106.90098	6 Nov 2009	21:37:25.083	−70.05	0.53	6.05
100612.58905	12 Jun 2010	14:08:14.137	135.01	−1.61	1.89
111024.60597	24 Oct 2011	14:32:36.098	100.54	−2.04	1.73
111103.86414	3 Nov 2011	20:44:22.554	100.63	2.06	3.40
111122.06618	22 Nov 2011	01:35:18.596	−143.67	1.62	0.98, 0.44

(T. Gjesteland, personal communication, 2013). On the contrary, multiple peaks with time separation of 1–4 ms were observed in many of the BATSE events, as reported in *Fishman et al.* [1994]. *Fishman et al.* [2011] report the observation of three evident double-peak events out of a sample of 53 TGFs detected by Fermi GBM, with peak time separation between 1.3 and 8.4 ms, indicating a multiple/single TGF ratio roughly consistent with that of AGILE. In addition to these events, there are possibilities for about another 10 TGFs being a superposition of closer pulses. The evidence for overlapping pulses in TGFs has already been reported in *Briggs et al.* [2010]. If closely spaced dim multiple peaks are not identified by the selection algorithms because of the limited number of counts, this could contribute to bias the duration distribution toward longer durations, as previously pointed out by *Grefenstette et al.* [2008], in addition to the dead time contribution discussed in section 5.3. Although *Gjesteland et al.* [2010] have shown that some of the BATSE

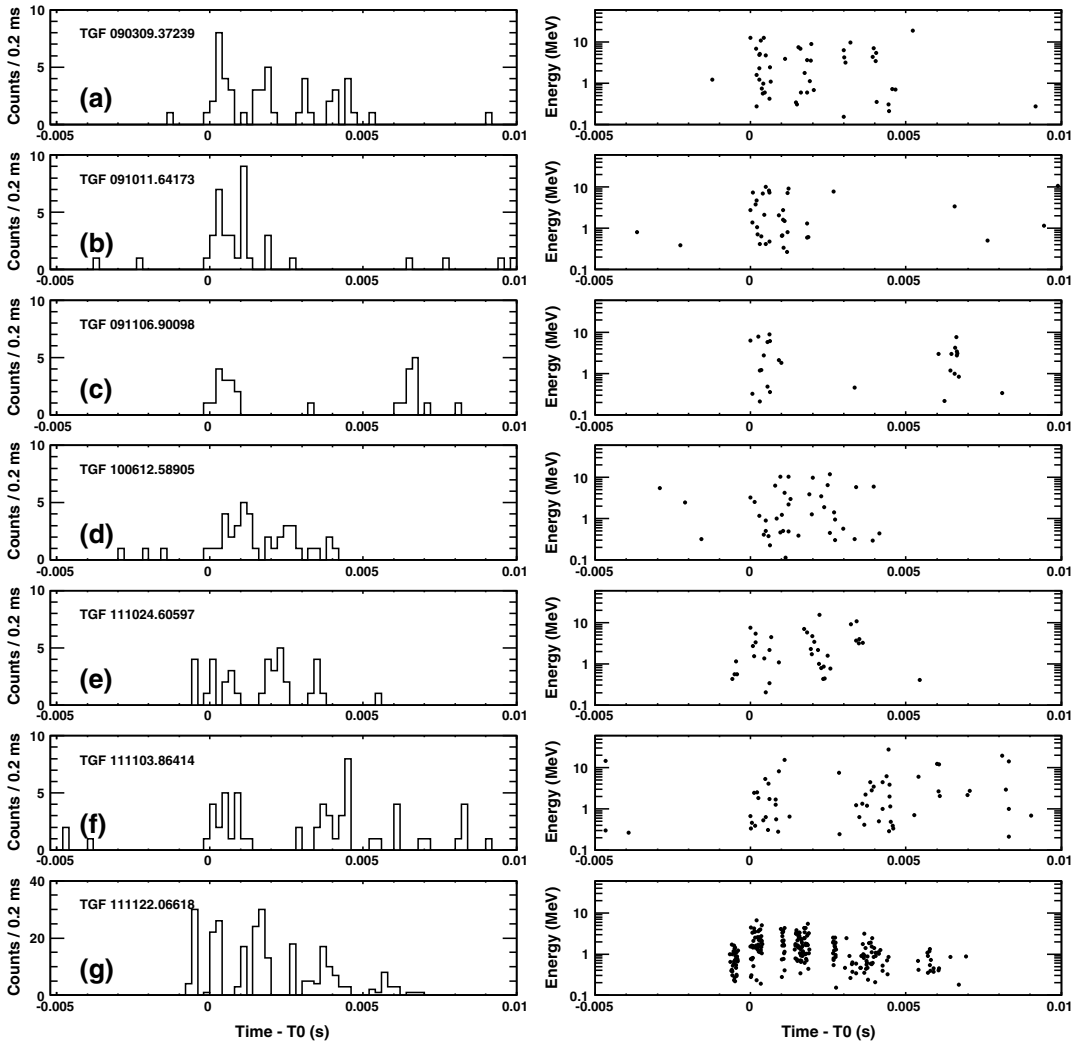

Figure 8. (first column) Light curves and (second column) energy versus time plot for the seven TGFs that evidence multiple peaks.

double-peak events can be explained by dead time effects, this does not apply to peaks separated by more than 1 ms. Therefore, the lack of multiple peak TGFs in the RHESSI data is remarkable and still needs a clear explanation.

5.5. Cumulative Spectrum

Spectral fitting of individual RHESSI and AGILE TGFs is typically hampered by the limited number of counts. On the other hand, cumulative spectra summing together photon's energies of several TGFs have already proven to be an effective tool to derive average properties of TGFs [*Dwyer and Smith*, 2005; *Grefenstette et al.*, 2009; *Marisaldi et al.*, 2010a; *Tavani et al.*, 2011a]. Based on Monte Carlo simulations of the Relativistic Runaway Electron Avalanche process at different atmospheric depths, *Dwyer and Smith* [2005] showed that the RHESSI TGF cumulative spectrum is compatible with a production altitude lower than 21 km, in agreement with measurements and theoretical modeling suggesting that TGFs are associated with lightning discharges at the cloud top altitude [*Cummer et al.*, 2005; *Williams et al.*, 2006] and ruling out the possible association between TGFs and sprites. These results are confirmed also by spectral fitting of individual BATSE TGFs, which is possible thanks to the larger number of counts, when an accurate model of the instrument dead time is considered [*Gjesteland et al.*, 2010]. *Xu et al.* [2012] report the agreement of the observed RHESSI cumulative spectrum also with the expected spectrum produced by lightning leaders [*Celestin and Pasko*, 2011], suggesting a production altitude of 12–13 km compatible with observations of positive intracloud lightning (+IC) associated to TGFs [*Stanley et al.*, 2006; *Shao et al.*, 2010]. *Marisaldi et al.* [2010a] computed the cumulative spectrum of the first 34 AGILE TGFs and showed that above 500 keV the spectrum can be fit with a power law with exponential cutoff model:

$$F(E) = KE^{-\alpha}e^{-\frac{E}{E_C}} \tag{2}$$

When the best fit result of this simple phenomenological model is convolved with the RHESSI detector response matrix, a good agreement with RHESSI experimental data is obtained. We note that the same functional form of equation (2) was used by *Gjesteland et al.* [2010] to fit BATSE individual spectra but assuming a fixed cutoff energy of 10 MeV. This assumption was appropriate for that study given the limited spectral resolution of BATSE data at high energy.

A new AGILE TGF cumulative spectrum was built summing the counts detected in a 10 ms time interval centered at the TGF start time for 228 single-pulse TGFs detected before 4 October 2011, when the first increase of the MCAL threshold took place. The background counts were integrated in the 1 s time interval centered at the TGF start time, excluding the central 200 ms time interval. The binning was arranged so that each bin is at least 3σ significant above the background. The spectrum was then fit in the range 0.4–30 MeV with the model described by equation (2), obtaining $\alpha = 0.20^{+0.12}_{-0.13}$, $E_C = 5.5^{+0.7}_{-0.6}$ MeV and a reduced χ^2 of 1.5 with 59 degrees of freedom. Figure 9 shows the unfolded, background-subtracted AGILE TGF cumulative photon spectrum. The data points have been corrected for the detector response matrix assuming the model spectrum described above. Figure 9 (green curve) also shows the model spectrum from *Dwyer and Smith* [2005] (D. Smith and J. Dwyer, personal communication, 2013) corresponding to the runaway breakdown model at a source altitude of 21 km, or 50 g/cm^2 atmospheric depth, normalized to the AGILE data integral in the range 1–10 MeV. This spectrum, which represents the best fit to RHESSI data, matches AGILE data quite well, therefore AGILE data support the low-altitude scenario for TGF production. However, we note that the AGILE best fit spectrum is harder than the RHESSI one. A power law with exponential cutoff fit of the RHESSI simulated data in the 0.4–30 MeV range yields $\alpha_{RH} = 0.04 \pm 0.03$, $E_{C,RH} = 4.2 \pm 0.2$ MeV as best fit parameters. A confidence level contour plot for AGILE fit parameters was built by letting α and E_C vary independently in an interval centered at the best fit values, and computing the corresponding chi-square statistics. The RHESSI simulations best fit parameters are not compatible at the 99% confidence level with the MCAL best fit parameters. This could be due to differences in the two instruments, AGILE being biased toward harder events than RHESSI because of the adopted trigger selection strategy, the detector's higher energy threshold and range. *Grefenstette et al.* [2009] have demonstrated an intrinsic spectral variability among TGFs, which is reasonable considering the different production altitudes and propagation paths to the spacecrafts, so a possible bias of AGILE toward harder events is to be expected. We note that the AC-induced dead time is not energy dependent; therefore, we do not expect a spectrum modification due to this effect, as in the case of BATSE [*Gjesteland et al.*, 2010]. However, if the peak of the emission is strongly suppressed by dead time, one can expect a softening of the spectrum due to Compton-reprocessed photons arriving late

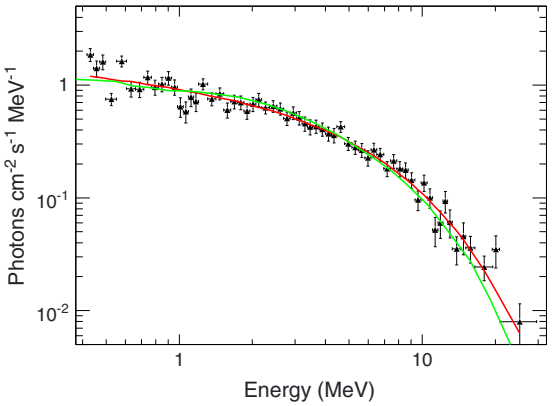

Figure 9. Cumulative photon spectrum of AGILE TGFs with maximum photon energy 30 MeV. AGILE data (black markers) have been corrected for the detector response matrix assuming a power law with exponential cutoff model (red curve). Vertical error bars are 1 standard deviation. It has also shown the model spectrum from *Dwyer and Smith* [2005] (green curve) corresponding to the runaway breakdown model at a source altitude of 21 km, which represents the best fit model to the RHESSI cumulative spectrum. The RHESSI model has been normalized to the AGILE data integral in the range 1–10 MeV.

with respect to the peak of the emission, therefore being less affected by dead time. This effect is significant for instruments sensitive below ≈ 300 keV, which is not the case of MCAL.

5.6. Sferics Correlation

Correlation between TGFs and sferics detected by WWLLN [*Rodger et al.*, 2009] have been searched. All the sferics in a 2 h interval centered at TGF time and within 2400 km (the maximum possible distance seen by the AGILE satellite at the horizon) from the subsatellite point were selected for analysis. For each selected sferic, the TGF time was corrected for propagation time at the sferic source assuming a source region at 15 km altitude. The sferic closest in time to the TGF was then extracted in three ranges of radial distance d from the subsatellite point: $d \leq 300$ km, $300 < d \leq 600$ km, $600 < d \leq 2400$ km. Distances greater than 1000 km were considered mostly for completeness, since *Connaughton et al.* [2013] found no true coincidences for distances larger than 1000 km. The algorithm was checked for correctness with an independent algorithm applied to the new RHESSI TGF catalog [*Gjesteland et al.*, 2012] and good agreement was found (T. Gjesteland, personal communication, 2013).

5.6.1. Search for Simultaneous Sferics

Among the 292 TGFs with WWLLN data available, only 14 TGFs have been associated to sferics within 20 ms. We tested the possibility that these associations could be due to random coincidences using the method described in *Connaughton et al.* [2010, 2013]: we searched for coincidences using the true TGF subsatellite location and a sample of 1000 artificial TGF times evenly distributed in a 1000 s interval centered at the true TGF time. We accumulate separately the random coincidences obtained for the distance regions mentioned above and for the time intervals $-20\,\text{ms} \leq \Delta t < -5\,\text{ms}$, $-5\,\text{ms} \leq \Delta t < +5\,\text{ms}$, $+5\,\text{ms} <= \Delta t < +20\,\text{ms}$, where Δt is the time difference between sferic and TGF, corrected for light travel time. All associations with the time stamps of the control sample are likely chance coincidences; therefore, this test allows to assess experimentally the likelihood that a sferic-TGF association is in fact a true coincidence or happened by chance. Assuming a $\geq 1\%$ chance probability to reject an association, we confirm the association for all eight TGFs with associated sferics closer than 600 km, and we reject all but one of the candidate associations at larger distances. This result confirms previous works in which associations to WWLLN sferics are reported up to a maximum distance of 600–800 km from the subsatellite point [*Hazelton et al.*, 2009; *Connaughton et al.*, 2013] and is compatible with the distribution of RHESSI TGF geolocations reported in *Cohen et al.* [2010]. However, we point out the case of the TGF detected on 14 April 2009 whose associated sferic is located at a distance of 1260 km from the subsatellite point, and the random coincidence test described above yields negative result. The main data of the TGFs with associated sferics are reported in Table 3; counts and t_{50} come from the maximum likelihood procedure described in section 5.2. Data for controversial associations are left separated from the rest of the sample. We note that all associations closer than 600 km but one have

Table 3. TGFs Associated With WWLLN Sferics Within 20 ms

Date	Time (UT)	Lon. (deg)	Lat. (deg)	Counts	t_{50} (ms)	Δt (ms)	d (km)
9 Mar 2009	08:56:15.206	−6.65	1.89	16.5 ± 4.2	0.21 ± 0.04	4.82	77
30 Mar 2009	00:14:14.093	112.88	−2.23	14.8 ± 3.9	0.18 ± 0.04	−3.72	143
17 Apr 2009	14:55:41.090	20.04	−1.64	17.1 ± 4.2	0.37 ± 0.06	2.14	131
10 Jan 2010	08:04:22.531	−174.25	1.89	29.4 ± 5.9	2.44 ± 0.40	4.49	237
12 Mar 2011	07:40:33.447	4.62	−2.44	12.8 ± 3.6	0.16 ± 0.03	2.39	482
17 Mar 2011	18:27:46.868	−4.74	2.42	11.7 ± 3.5	0.12 ± 0.03	2.42	290
3 Apr 2012	11:13:18.313	133.44	0.61	14.7 ± 3.9	0.35 ± 0.07	−14.80	100
14 Apr 2009	22:21:57.882	28.65	−1.62	30.1 ± 5.6	0.46 ± 0.06	8.00	1263

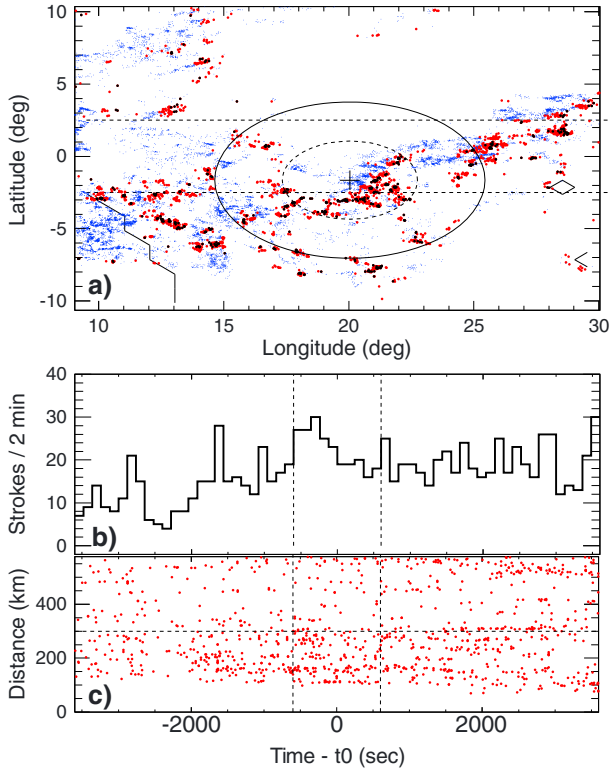

Figure 10. WWLLN sferics distributions related to TGF detected on 17 April 2009, exhibiting the closest WWLLN association in time (2.145 ms). (a) Geographical distribution; the cross is the subsatellite point at trigger time; the dashed and continuous circles are 300 and 600 km in radius, respectively. Small blue dots are sferics detected during all the day; red dots are sferics within ±1 h from trigger; black dots are sferics within ±10 min from trigger. (b) Rate of sferics within 600 km from the subsatellite point at trigger time. (c) Distance with respect to subsatellite point at trigger time for sferics within ±1 h from trigger.

$|\Delta t| < 5$ ms. Interestingly, the TGF detected on 9 March 2009 is a multipeaked TGF, reported in Table 2 and Figure 8, and the associated sferic, which is 4.8 ms after the first peak, happens to be simultaneous to the last peak of the sequence. This peak is too weak to be identified as an independent event by the trigger search but could be responsible for the detected radio emission.

We remarkably note that no sferic simultaneous to a TGF was detected, i.e., within a 200 μs time interval according to the definition of simultaneity proposed in *Connaughton et al.* [2013]. Only one candidate was present, with a sferic distance larger than 1000 km, but it was rejected by the random coincidence test. This lack of simultaneous matches can be explained according to the duration distribution of AGILE TGFs, which has a median value of a factor of 2.6 that of Fermi, as discussed in section 5.2. According to *Connaughton et al.* [2013], the probability to observe a sferic simultaneous with a TGF increases as the TGF duration decreases. This is explained as the sferic being the very low frequency (VLF) signature of the electron avalanche producing the TGF itself, a possibility previously suggested in *Cummer et al.* [2011] and *Dwyer* [2012] and extensively developed in *Dwyer and Cummer* [2013]. According to this model, a shorter TGF duration corresponds to a higher peak current moment, hence a higher power radiated in the VLF range and therefore a higher probability to be detected by a ground-based lightning detection network. Considering Figure 3 of *Connaughton et al.* [2013], the probability of a simultaneous WWLLN association with Fermi TGFs is 10% for TGFs with t_{50} in the interval 120–190 μs and is zero above. These calculations refer to photons above 300 keV, which is an appropriate cut considering the MCAL energy threshold. Only 31 AGILE TGFs have t_{50} in the 120–190 μs interval, and none has shorter duration. Of these 31 events we have WWLLN data available for 27 of them. We would expect then to find two to three simultaneous detections, while we observed zero. The binomial probability of observing zero positive events on 27 extractions with 0.1 probability is 5.8%, a low but not negligible value. Moreover, we note that 12 of these events are above Africa,

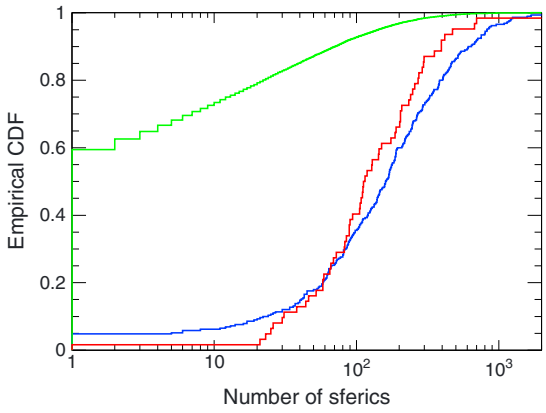

Figure 11. Empirical cumulative distribution functions (CDF) for the number of sferics detected within a radius of 600 km from the subsatellite point in a 20 min time interval centered at the TGF time (N_{600}) for AGILE TGFs (blue curve), a sample of the new RHESSI TGFs with latitude lower than 10° in absolute value (red curve), and a sample of AGILE positions extracted at random times (green curve).

where WWLLN detection efficiency is on average about 40% the maximum value observed, for example, in the continental U.S. *Hutchins et al.* [2012].

Motivated by this lack of simultaneous detections, we decided to check whether our selection criteria were artificially biasing our TGF sample toward longer durations, although dead time modeling suggests that the detection of short events should be suppressed. Our working hypothesis was that shorter TGFs, more likely associated to simultaneous sferics, could not be identified by the selection criteria described in section 3. If we were missing a significant population of short-duration TGFs, a large fraction of them should be associated to simultaneous sferics. We therefore searched for sferics correlation in a subset of 84,000 clusters for which we have WWLLN data available. We recall here that cluster selection is the very first step of our trigger search algorithm, requiring only a minimum of six counts in a 1 ms time window, without any additional selection criteria. Among this large sample, we found only three clusters with associated sferics within 200μs time interval, but with distances to the subsatellite point larger than 1100 km, and subsequently rejected by the random coincidence test described above. Therefore, we conclude that our selection strategy is not neglecting a significant population of short-duration TGFs. The lack of sensitivity to short-duration TGFs is intrinsic to the instrument and not related to the adopted selection criteria. The reason for this is the dead time induced by the AC, as already pointed out in sections 4 and 5.2.

5.6.2. Lightning Activity Associated to TGFs

In addition to the search for simultaneous correlations, we analyzed the WWLLN data to assess the overall lightning activity in the region surrounding the TGF. We considered the distance bins (with boundaries at 300, 600, and 2400 km) mentioned above, and the temporal bins defined as follows: −60 to −10, −10 to +10, and +10 to +60 min with respect to the TGF time. These time and distance boundaries define a 3 × 3 matrix which we fill in with the WWLLN sferics occurrences for every TGF. Figure 10 shows the WWLLN detection in the reference time and spatial intervals for the TGF detected on 17 April 2009.

According to the above procedure we compute the number of sferics detected within a radius of 600 km in a 20 min time interval centered at the TGF time, N_{600} hereafter, that we consider a good observable to quantify the regional lightning activity surrounding the TGF. To check in an independent way the goodness of our selection algorithm, we computed the same quantity for a subset of AGILE positions extracted at random times in the reference time period (the control sample). A quantitative comparison between the two distributions can be made by means of the Kolmogorov Smirnov (KS) test, testing the null hypothesis that the two samples come from the same parent distribution. The test was applied to 100 subsamples extracted randomly from the control sample (bootstrapping), each containing 292 values in order to be comparable in size with the TGF sample, and the subsequent application of the KS test. The maximum distance between the empirical cumulative distributions of the two samples was never found smaller than 0.68, as it is evident from Figure 11, with a corresponding negligible p value indicating that the null hypothesis can be rejected. This apparently trivial result is a quantitative demonstration of the fact that TGFs come from regions of enhanced lightning activity but can also serve as a test procedure to compare TGF samples detected by different satellites or with different selection criteria.

For this purpose we applied the same test to AGILE and the new RHESSI TGFs, the enhanced RHESSI TGF sample described in *Gjesteland et al.* [2012] (T. Gjesteland, personal communication, 2013). We selected 61 new RHESSI TGFs with latitude lower than 10° in absolute value and with WWLLN data available. The latitude belt selection was introduced to work on a sample more compliant to the AGILE orbit, in order to avoid a bias in the N_{600} distribution due to latitude-related thunderstorm characteristics and WWLLN sensitivity issues [*Hutchins et al.*, 2012]. A narrower selection in latitude would result in much fewer events, making the KS test less significant. Figure 11 shows the empirical cumulative distribution of N_{600} for both AGILE, new

RHESSI, and AGILE-simulated samples. We performed the same bootstrap test as before, extracting 1000 random subsamples from the AGILE distribution, each containing 61 events, and comparing them to the RHESSI N_{600} distribution by means of the KS test. In 86% of the cases the p value is greater than 0.05 (mean value 0.35), suggesting that we cannot reject the null hypothesis that both samples come from the same parent distribution with a 95% confidence level. This test points out that there are no macroscopic differences in the lightning activity, as quantified by the N_{600} parameter, of the thunderstorms conducive to the production of TGFs detected by the two instruments.

6. Summary and Conclusions

We present here the characteristics of 308 TGFs detected by AGILE during the period March 2009 to July 2012 and selected to have the maximum photon energy up to 30 MeV. Thanks to its very low inclination orbit, AGILE provides the largest TGF surface detection rate density in the equatorial region available up to now, a value only recently reached by Fermi-GBM in the untriggered mode. The adopted selection strategy requires the onboard trigger plus a set of cuts on intensity, hardness ratio, and topology. In general, the AGILE TGF properties well match those reported by RHESSI and Fermi-GBM, with few remarkable exceptions. The main results obtained can be summarized as follows:

1. The average detection rate is ~0.3 TGFs/d, when the AGILE exposure is properly accounted for. Excluding the request for the onboard trigger and applying the other selection criteria to the available photon by photon data result in a modest increase ($< 10\%$) in the number of events, suggesting that the onboard trigger logic on time windows < 1 ms effectively triggers on the vast majority of the events.
2. The AC-induced dead time is a key factor to understand important TGF properties such as duration and intensity distributions; detailed simulations and modeling allows to take this effect properly into account. This explains also why no Terrestrial Electron Beam has been detected by AGILE.
3. The duration distribution is biased toward larger values than RHESSI and Fermi-GBM because of the AC-induced dead time, which prevents the detection of TGFs shorter than $\approx 100\,\mu$s.
4. The intensity distribution is consistent with a power law fluence distribution with index $\lambda \approx 2.4$ for large fluences, compatible with previous studies [*Østgaard et al.*, 2012; *Tierney et al.*, 2013]. Remarkably, all three operating TGF detectors, with different characteristics and different analysis methods, point toward the same result. The observed roll-off for low fluence values is possibly due to selection effects caused by the selection cut on hardness ratio.
5. The number of AGILE TGFs made of multiple peaks separated by a few milliseconds is about 2% of the sample. This fraction may be even larger if low-intensity peaks, not recognized as independent TGFs by the selection algorithm, are considered. While this fraction is roughly consistent with Fermi-GBM results, this does not seem to be the case for RHESSI. This point deserves additional investigation to disentangle possible instrumental effects or different population properties.
6. The cumulative spectrum can be fit with a power law with exponential cutoff model and is quite in agreement with RHESSI results, further supporting, with an independent data set, the scenario of low-altitude production. However, the spectrum is harder than RHESSI-simulated spectrum, suggesting a possible selection bias toward harder events.
7. No WWLLN sferics simultaneous to TGFs were detected. This is consistent with the fact that the detection of TGFs shorter than $\approx 100\,\mu$s is suppressed by dead time effects. Results reported in *Connaughton et al.* [2013] suggest that we should expect two to three simultaneous detections, but this estimate does not account for the lower efficiency of WWLLN above equatorial Africa, where a large fraction of AGILE events is detected.
8. Despite the lack of simultaneous sferics, we used the number of WWLLN sferics detected in a spatial region and temporal interval centered at the subsatellite point and TGF time as an estimator of the overall lightning activity of the thunderstorm system conducive to TGF production. We show that, as far as this parameter is concerned, AGILE and RHESSI TGF samples are compatible with the same parent distribution.

An online version of the AGILE TGF catalog below 30 MeV is accessible from the ASI Science Data Center website http://www.asdc.asi.it/mcaltgfcat/ as an interactive web table, including access to available TGF light curves.

Acknowledgments
AGILE is a mission of the Italian Space Agency (ASI), with coparticipation of INAF (Istituto Nazionale di Astrofisica) and INFN (Istituto Nazionale di Fisica Nucleare). This work was carried out in the frame of the ASI-INAF agreement I/028/12/0. M. Marisaldi thanks Thomas Gjesteland and Nikolai Østgaard for fruitful discussions during his visiting period at the University of Bergen, Norway. This study was supported by the European Research Council under the European Unions Seventh Framework Programme (FP7/2007-2013)/ERC grant agreement 320839 and the Research Council of Norway under contracts 208028/F50, 216872/F50, and 223252/F50 (CoE). We thank the institutions contributing to WWLLN (http://wwlln.net/).

Robert Lysak thanks the reviewers for their assistance in evaluating this paper.

References

Argan, A., et al. (2004), The data handling system for the AGILE satellite, in *Conference Record of the IEEE Nuclear Science Symposium, October 16–22, 2004, Rome, Italy*, pp. 371–375.

Briggs, M. S., et al. (2010), First results on terrestrial gamma ray flashes from the Fermi Gamma-Ray Burst Monitor, *J. Geophys. Res.*, *115*, A07323, doi:10.1029/2009JA015242.

Briggs, M. S., et al. (2011), Electron-positron beams from terrestrial lightning observed with Fermi GBM, *Geophys. Res. Lett.*, *38*, L02808, doi:10.1029/2010GL046259.

Briggs, M. S., et al. (2013), Terrestrial gamma-ray flashes in the Fermi era: Improved observations and analysis methods, *J. Geophys. Res. Space Physics*, *118*, 3805–3830, doi:10.1002/jgra.50205.

Brun, R., and F. Carminati (1993), GEANT—Detector description and simulation tool, CERN Program Library Long Writeup W5013, CERN Geneva, Switzerland.

Celestin, S., and V. P. Pasko (2011), Energy and fluxes of thermal runaway electrons produced by exponential growth of streamers during the stepping of lightning leaders and in transient luminous events, *J. Geophys. Res.*, *116*, A03315, doi:10.1029/2010JA016260.

Celestin, S., W. Xu, and V. P. Pasko (2012), Terrestrial gamma ray flashes with energies up to 100 MeV produced by nonequilibrium acceleration of electrons in lightning, *J. Geophys. Res.*, *117*, A05315, doi:10.1029/2012JA017535.

Cocco, V., F. Longo, and M. Tavani (2002), Simulation of the AGILE gamma-ray imaging detector performance: Part II, *Nucl. Instrum. Methods Phys. Res. A*, *486*, 623–638, doi:10.1016/S0168-9002(01)02160-X.

Cohen, M. B., U. S. Inan, R. K. Said, and T. Gjestland (2010), Geolocation of terrestrial gamma-ray flash source lightning, *Geophys. Res. Lett.*, *37*, L02801, doi:10.1029/2009GL041753.

Collier, A. B., T. Gjesteland, and N. Østgaard (2011), Assessing the power law distribution of TGFs, *J. Geophys. Res.*, *116*, A10320, doi:10.1029/2011JA016612.

Connaughton, V., et al. (2010), Associations between Fermi Gamma-Ray Burst Monitor terrestrial gamma ray flashes and sferics from the World Wide Lightning Location Network, *J. Geophys. Res.*, *115*, A12307, doi:10.1029/2010JA015681.

Connaughton, V., et al. (2013), Radio signals from electron beams in terrestrial gamma ray flashes, *J. Geophys. Res. Space Physics*, *118*, 2313–2320, doi:10.1029/2012JA018288.

Crawford, D. F., D. L. Jauncey, and H. S. Murdoch (1970), Maximum-likelihood estimation of the slope from number-flux counts of radio sources, *Astrophys. J.*, *162*, 405, doi:10.1086/150672.

Cummer, S. A., Y. Zhai, W. Hu, D. M. Smith, L. I. Lopez, and M. A. Stanley (2005), Measurements and implications of the relationship between lightning and terrestrial gamma ray flashes, *Geophys. Res. Lett.*, *32*, L08811, doi:10.1029/2005GL022778.

Cummer, S. A., G. Lu, M. S. Briggs, V. Connaughton, S. Xiong, G. J. Fishman, and J. R. Dwyer (2011), The lightning-TGF relationship on microsecond timescales, *Geophys. Res. Lett.*, *38*, L14810, doi:10.1029/2011GL048099.

Dwyer, J. R. (2012), The relativistic feedback discharge model of terrestrial gamma ray flashes, *J. Geophys. Res.*, *117*, A02308, doi:10.1029/2011JA017160.

Dwyer, J. R., and S. A. Cummer (2013), Radio emissions from terrestrial gamma-ray flashes, *J. Geophys. Res. Space Physics*, *118*, 3769–3790, doi:10.1002/jgra.50188.

Dwyer, J. R., and D. M. Smith (2005), A comparison between Monte Carlo simulations of runaway breakdown and terrestrial gamma-ray flash observations, *Geophys. Res. Lett.*, *32*, L22804, doi:10.1029/2005GL023848.

Dwyer, J. R., B. W. Grefenstette, and D. M. Smith (2008), High-energy electron beams launched into space by thunderstorms, *Geophys. Res. Lett.*, *35*, L02815, doi:10.1029/2007GL032430.

Dwyer, J. R., D. M. Smith, and S. A. Cummer (2012), High-energy atmospheric physics: Terrestrial gamma-ray flashes and related phenomena, *Space Sci. Rev.*, *173*, 133–196, doi:10.1007/s11214-012-9894-0.

Feroci, M., et al. (2007), SuperAGILE: The hard X-ray imager for the AGILE space mission, *Nucl. Instrum. Methods Phys. Res. A*, *581*, 728–754, doi:10.1016/j.nima.2007.07.147.

Fishman, G. J., et al. (2011), Temporal properties of the terrestrial gamma-ray flashes from the Gamma-Ray Burst Monitor on the Fermi Observatory, *J. Geophys. Res.*, *116*, A07304, doi:10.1029/2010JA016084.

Fishman, G. J., et al. (1994), Discovery of intense gamma-ray flashes of atmospheric origin, *Science*, *264*, 1313–1316.

Fuschino, F., et al. (2008), Search of GRB with AGILE Minicalorimeter, *Nucl. Instrum. Methods Phys. Res. A*, *588*, 17–21, doi:10.1016/j.nima.2008.01.004.

Fuschino, F., et al. (2011), High spatial resolution correlation of AGILE TGFs and global lightning activity above the equatorial belt, *Geophys. Res. Lett.*, *38*, L14806, doi:10.1029/2011GL047817.

Galli, M., et al. (2013), AGILE mini-calorimeter gamma-ray burst catalog, *Astron. Astrophys.*, *553*, A33, doi:10.1051/0004-6361/201220833.

Gjesteland, T., N. Østgaard, P. H. Connell, J. Stadsnes, and G. J. Fishman (2010), Effects of dead time losses on terrestrial gamma ray flash measurements with the Burst and Transient Source Experiment, *J. Geophys. Res.*, *115*, A00E21, doi:10.1029/2009JA014578.

Gjesteland, T., N. Østgaard, A. B. Collier, B. E. Carlson, M. B. Cohen, and N. G. Lehtinen (2011), Confining the angular distribution of terrestrial gamma ray flash emission, *J. Geophys. Res.*, *116*, A11313, doi:10.1029/2011JA016716.

Gjesteland, T., N. Østgaard, A. B. Collier, B. E. Carlson, C. Eyles, and D. M. Smith (2012), A new method reveals more TGFs in the RHESSI data, *Geophys. Res. Lett.*, *39*, L05102, doi:10.1029/2012GL050899.

Grefenstette, B. W., D. M. Smith, J. R. Dwyer, and G. J. Fishman (2008), Time evolution of terrestrial gamma ray flashes, *Geophys. Res. Lett.*, *35*, L06802, doi:10.1029/2007GL032922.

Grefenstette, B. W., D. M. Smith, B. J. Hazelton, and L. I. Lopez (2009), First RHESSI terrestrial gamma ray flash catalog, *J. Geophys. Res.*, *114*, A02314, doi:10.1029/2008JA013721.

Hazelton, B. J., B. W. Grefenstette, D. M. Smith, J. R. Dwyer, X.-M. Shao, S. A. Cummer, T. Chronis, E. H. Lay, and R. H. Holzworth (2009), Spectral dependence of terrestrial gamma-ray flashes on source distance, *Geophys. Res. Lett.*, *36*, L01108, doi:10.1029/2008GL035906.

Hurley, K., et al. (2013), The interplanetary network supplement to the Fermi GBM Catalog of cosmic Gamma-Ray Bursts, *ArXiv e-prints*.

Hutchins, M. L., R. H. Holzworth, J. B. Brundell, and C. J. Rodger (2012), Relative detection efficiency of the World Wide Lightning Location Network, *Radio Sci.*, *47*, RS6005, doi:10.1029/2012RS005049.

Koshut, T. M., W. S. Paciesas, C. Kouveliotou, J. van Paradijs, G. N. Pendleton, G. J. Fishman, and C. A. Meegan (1996), Systematic effects on duration measurements of gamma-ray bursts, *Astrophys. J.*, *463*, 570, doi:10.1086/177272.

Labanti, C., et al. (2009), Design and construction of the mini-calorimeter of the AGILE satellite, *Nucl. Instrum. Methods Phys. Res. A*, *598*, 470–479, doi:10.1016/j.nima.2008.09.021.

Longo, F., V. Cocco, and M. Tavani (2002), Simulation of the AGILE gamma-ray imaging detector performance: Part I, *Nucl. Instrum. Methods Phys. Res. A*, *486*, 610–622, doi:10.1016/S0168-9002(01)02159-3.

Marisaldi, M., et al. (2008), Gamma-ray burst detection with the AGILE mini-calorimeter, *Astron. Astrophys.*, *490*, 1151–1156, doi:10.1051/0004-6361:200810562.

Marisaldi, M., et al. (2010a), Detection of terrestrial gamma ray flashes up to 40 MeV by the AGILE satellite, *J. Geophys. Res.*, *115*, A00E13, doi:10.1029/2009JA014502.

Marisaldi, M., et al. (2010b), Gamma-ray localization of terrestrial gamma-ray flashes, *Phys. Rev. Lett.*, *105*(12), 128501, doi:10.1103/PhysRevLett.105.128501.

Marisaldi, M., et al. (2012), Observational evidence of two different populations of terrestrial gamma-ray flashes, EGU General Assembly 2012, 22–27 April, 2012, Vienna, Austria, 9465 pp.

Østgaard, N., T. Gjesteland, J. Stadsnes, P. H. Connell, and B. Carlson (2008), Production altitude and time delays of the terrestrial gamma flashes: Revisiting the Burst and Transient Source Experiment spectra, *J. Geophys. Res.*, *113*, A02307, doi:10.1029/2007JA012618.

Østgaard, N., T. Gjesteland, R. S. Hansen, A. B. Collier, and B. Carlson (2012), The true fluence distribution of terrestrial gamma flashes at satellite altitude, *J. Geophys. Res.*, *117*, A03327, doi:10.1029/2011JA017365.

Østgaard, N., T. Gjesteland, B. E. Carlson, A. B. Collier, S. A. Cummer, G. Lu, and H. J. Christian (2013), Simultaneous observations of optical lightning and terrestrial gamma ray flash from space, *Geophys. Res. Lett.*, *40*, 2423–2426, doi:10.1002/grl.50466.

Pal'shin, V. D., et al. (2013), IPN localizations of Konus short gamma-ray bursts, *ArXiv e-prints*.

Perotti, F., M. Fiorini, S. Incorvaia, E. Mattaini, and E. Sant'Ambrogio (2006), The AGILE anticoincidence detector, *Nucl. Instrum. Methods Phys. Res. A*, *556*, 228–236, doi:10.1016/j.nima.2005.10.016.

Prest, M., G. Barbiellini, G. Bordignon, G. Fedel, F. Liello, F. Longo, C. Pontoni, and E. Vallazza (2003), The AGILE silicon tracker: An innovative $/\gamma$-ray instrument for space, *Nucl. Instrum. Methods Phys. Res. A*, *501*, 280–287, doi:10.1016/S0168-9002(02)02047-8.

Rodger, C. J., J. B. Brundell, R. H. Holzworth, and E. H. Lay (2009), Growing detection efficiency of the world wide lightning location network, in *Proceedings of the Workshop on Coupling of Thunderstorms and Lightning Discharges to Near-Earth Space, Am. Inst. of Phys. Conf. Ser.*, vol. 1118, pp. 15–20, doi:10.1063/1.3137706.

Shao, X.-M., T. Hamlin, and D. M. Smith (2010), A closer examination of terrestrial gamma-ray flash-related lightning processes, *J. Geophys. Res.*, *115*, A00E30, doi:10.1029/2009JA014835.

Smith, D. M., B. J. Hazelton, B. W. Grefenstette, J. R. Dwyer, R. H. Holzworth, and E. H. Lay (2010), Terrestrial gamma ray flashes correlated to storm phase and tropopause height, *J. Geophys. Res.*, *115*, A00E49, doi:10.1029/2009JA014853.

Smith, D. M., et al. (2005), Terrestrial gamma-ray flashes observed up to 20 MeV, *Science*, *307*, 1085–1088.

Stanley, M. A., X.-M. Shao, D. M. Smith, L. I. Lopez, M. B. Pongratz, J. D. Harlin, M. Stock, and A. Regan (2006), A link between terrestrial gamma-ray flashes and intracloud lightning discharges, *Geophys. Res. Lett.*, *33*, L06803, doi:10.1029/2005GL025537.

Tavani, M., et al. (2009), The AGILE Mission, *Astron. Astrophys.*, *502*, 995–1013, doi:10.1051/0004-6361/200810527.

Tavani, M., et al. (2011a), Terrestrial gamma-ray flashes as powerful particle accelerators, *Phys. Rev. Lett.*, *106*(1), 018501, doi:10.1103/PhysRevLett.106.018501.

Tavani, M., et al. (2011b), Terrestrial gamma-ray flashes at the highest energies as detected by AGILE, Abstract AE24A-06 presented at 2011 Fall Meeting, AGU, San Francisco, Calif.

Tierney, D., et al. (2013), Fluence distribution of terrestrial gamma ray flashes observed by the Fermi Gamma-Ray Burst Monitor, *J. Geophys. Res. Space Physics*, *118*, 6644–6650, doi:10.1002/jgra.50580.

Williams, E., et al. (2006), Lightning flashes conducive to the production and escape of gamma radiation to space, *J. Geophys. Res.*, *111*, D16209, doi:10.1029/2005JD006447.

Xu, W., S. Celestin, and V. P. Pasko (2012), Source altitudes of terrestrial gamma-ray flashes produced by lightning leaders, *Geophys. Res. Lett.*, *39*, L08801, doi:10.1029/2012GL051351.